Near-Field Focusing Multibeam Geodesic Lens Antenna for Stable Aggregate Gain in Far-Field

Omar Orgeira, Germán León, Nelson J. G. Fonseca, *Senior Member, IEEE*, Pedro Mongelos, and Oscar Quevedo-Teruel, *Senior Member, IEEE*

Abstract—The millimeter-wave band is a very attractive frequency band for the new generations of mobile cellular networks, i.e. 5G and 6G, due to its potential to support extremely high data rate transmissions. Innovative antenna solutions are needed to relieve the higher free space attenuation at these frequencies. Here, we propose a multibeam antenna based on a geodesic lens with stable aggregate gain characteristics in far-field. An analytical model based on the physical path of the rays inside the lens is applied to achieve the field distribution in the aperture of the lens. This method is used to find the profile of a near-field focusing lens with a widened beam in the far-field. As a proof-of-concept, a seven-beam antenna has been designed. Thanks to the rotational symmetry of the geodesic lens, the antenna beams present similar characteristics over an extended sectorial coverage. The lens antenna has been manufactured and its near-field focusing features were validated. The prototype has been assessed also in the far-field with a good agreement between model, simulations and measurements. The main novelty of this prototype is to achieve a multiple beam coverage within $\pm 67°$ in the H-plane and $\pm 20°$ in the E-plane, with a gain roll-off smaller than 2 dB at 30 GHz and smaller than 3 dB at 35 GHz. These results validate the stable aggregate gain characteristics in far-field of the proposed solution.

Index Terms—Geodesic lens, lens antenna, 5G, 6G, millimetre-wave band, multibeam antenna, stable coverage.

I. INTRODUCTION

THE new mobile cellular network generations, including 5G and 6G, demand extremely high data rate to support ultra high-definition multimedia streaming or backhaul services [1]. The necessary bandwidth for these services can be achieved in the millimeter-wave (mmWave) band [2]. Thanks to the development of novel antennas and massive-array signal processing techniques, this technology recently started with fixed wireless access [3]. Highly directive antennas are required to overcome free space propagation and feeding network losses [4]. The main candidates are planar array antennas [5], reflectarrays [6] and lens antennas [7]. With adequate beamforming techniques, these antenna solutions are capable of generating a number of independent beams to cover a predefined angular range, enabling spectrum reuse over the field of view [8].

In the mmWave band, quasi-optical systems are of interest to provide large apertures and associated high gain. Various solutions have been developed, based on pillbox antennas [9]–[11], Rotman lenses [12]–[15] and Luneburg lenses [16], [17]. In these developments, the dielectric losses are often mitigated using substrate integrated waveguide (SIW) technology [18]. However, some applications require highly efficient designs and beamforming solutions with propagation in the air are preferred. Fully-metallic parallel plate waveguide (PPW) present very low transmission losses, moderate cost and enough flexibility to feed and develop lens antennas [19], [20]. In [21], [22], a ray-tracing analysis of a continuous delay-lens PPW beamformer based on the propagation inside a transversal cavity was validated, with good accuracy and significant reduction in the computational effort. This method has been used in [23] to enhance the beam performance. With a similar aim, fully-metallic Luneburg lens antennas based on metasurfaces have been also proposed [24]–[28]. These works use metallic nails or holes to synthesize a graded refractive index. The Luneburg lens is attractive for its rotationally symmetric properties [29], enabling a wide sectorial coverage where other quasi-optical beamformers are typically limited to $\pm 50°$ [30].

A PPW propagation can be analyzed using a dyadic Green's function [31] or modelled with rays confined between the plates that propagate following a geodesic curve [32], [33]. This method was used to design antennas with different elevation angles [34], [35]. The scanning properties of Rinehart-Luneburg geodesic lenses have been recently revisited [36]–[41]. These antennas present narrow pencil beams with a crossover point between two adjacent beams typically 6 dB below the beam peak, due to the physical separation between feeding points. This leads to strong aggregate gain variations across the sectorial coverage, possibly resulting in significant variations in link performance, which are not desirable in future 5G/6G communications. To overcome this issue, the

Corresponding author: G. León (email: gleon@uniovi.es).

O. Orgeira and O. Quevedo-Teruel are with the Division of Electromagnetic Engineering, School of Electrical Engineering, KTH Royal Institute of Technology, 100 44 Stockholm, Sweden (e-mail: omaroa@kth.se, oscarqt@kth.se).

G. León is with the Department of Electrical Engineering, University of Oviedo, 33204 Gijón, Spain (e-mail: gleon@uniovi.es).

N. J. G. Fonseca is with the Antenna and Sub-Millimetre Waves Section, European Space Agency, 2200 AG, Noordwijk, The Netherlands (e-mail: nelson.fonseca@esa.int).

P. Mongelos is an independent researcher in the field of Aerospace Engineering. (e-mail: pedro.mongelos@gmail.com).

width of the beam can be widened by modifying (de-focusing) the Luneburg lens [42], [43].

The goal of this work is to design a multibeam geodesic lens antenna (GLA) at mmWave frequencies with relatively uniform patterns in the H-plane to reduce gain roll-off over the service area. In section II, an analytical model to study a geodesic lens with rotational symmetry is described. This algorithm is a combination of a ray tracing model [33], [44] to study the propagation inside the lens and a source array model to calculate the electric field outside the lens [22], [40]. A preliminary version of this model was proposed in [45]. Here, we include also the feed position, so spillover losses can be taken into account improving the model accuracy. In Section III.A, this model has been used to find a GLA with a beamwidth of 20º and a gain roll-off below 2 dB, within the near-field (NF) focusing lens family [44]. This proof-of-concept has been designed at 30 GHz for easy comparison with other designs. In Section III.B, the designed antenna has been manufactured and the prototype has been validated in the NF, demonstrating its focusing properties. In Section III.C, the radiation characteristics are evaluated in the far-field (FF). The results show that the gain drop at the crossover point is less than 2 dB at 30 GHz within the angular range of $\pm 67°$ in the H-plane. Section IV summarizes the conclusions reached with this work.

II. ANALYTICAL MODEL

A. Ray tracing inside the geodesic lens

Each point of a rotationally symmetric geodesic lens, with respect to the Z-axis, can be described by a radial coordinate ρ, an angular coordinate ϕ and the value of the function $s(\rho)$, that represents the length on the geodesic surface, measured along the meridian from the axis of symmetry to the given point, instead of the coordinate z. This approach to describe geodesic lenses was introduced by Rinehart [36] to simplify the analytical expressions.
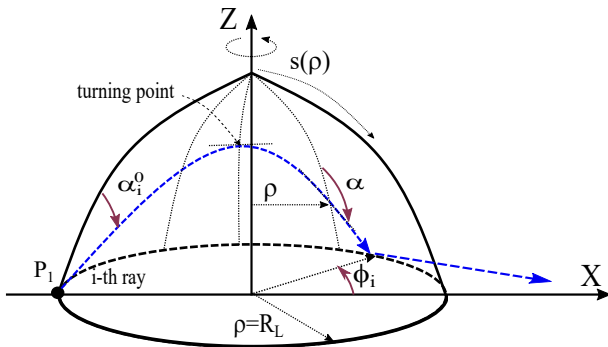

Fig. 1: Schematic representation of the ray tracing model including the propagation inside the geodesic lens.

In Fig. 1, the trajectory of a ray inside a geodesic lens is illustrated. The ray emerges from a point source $P_1[\rho_1 = R_L, \phi = \pi]$ with an angle α_i^0 with respect to the meridian and passes through the lens maintaining its angular momentum L_i constant [44]. This angular momentum is given by:

$$L_i = \rho \sin \alpha = R_L \sin \alpha_i^0 = R_L \sin(\pi - \alpha_i^0), \quad (1)$$

where α is the angle between the ray path and the meridian (pointing towards the centre).

The line element of the ray trajectory, $d\sigma$, fulfills these two equations [44]:

$$d\sigma = \frac{rd\phi}{\sin \alpha} \quad (2)$$

$$d\sigma^2 = d\rho^2 + dz^2 + \rho^2 d\phi^2 = ds^2 + \rho^2 d\phi^2 \quad (3)$$

From these relations, the differential equation that describes the ray trajectory inside the lens can be deduced:

$$d\phi = \pm \frac{L_i s'(\rho) d\rho}{\rho \sqrt{\rho^2 - L_i^2}} \quad (4)$$

where $s'(\rho) = \frac{ds(\rho)}{d\rho}$.

Returning to (1), a set of rays rises from P_1 with angles α_i^0 and travel along the geodesic lens. While α_i increases, ρ decreases until the ray reaches the turning point where $\alpha_i = \pi/2$ and $\rho = L_i$. After that point, the value of ρ increases until it leaves the lens at the point $\rho = R_L$ and ϕ_i, which can be obtained integrating (4):

$$\int_{-\pi}^{\phi_i} d\phi_i = -\int_{R_L}^{L_i} \frac{L_i s'(\rho) d\rho}{\rho \sqrt{\rho^2 - L_i^2}} + \int_{L_i}^{R_L} \frac{L_i s'(\rho) d\rho}{\rho \sqrt{\rho^2 - L_i^2}} \quad (5)$$

The signs have been chosen so that ϕ_i shall be an increasing function and $s(\rho)$ is also an increasing function, so $s'(\rho)$ is always positive. Equation (5) can be simplified:

$$\phi_i = 2 \cdot \int_{L_i}^{R_L} \frac{L_i s'(\rho) d\rho}{\rho \sqrt{\rho^2 - L_i^2}} - \pi \quad (6)$$

The total traveled distance of the i-th ray is:

$$\sigma_i = 2 \cdot \int_{L_i}^{R_L} \sqrt{s'(\rho)^2 \cdot \left(1 + \frac{L_i^2}{\rho^2 - L_i^2}\right)} d\rho \quad (7)$$

Finally, the ray leaves the lens at $\rho = R_L$ forming an angle $\pi - \alpha_i^0$ with the meridian (Fig. 2), following the last term of the equality (1).
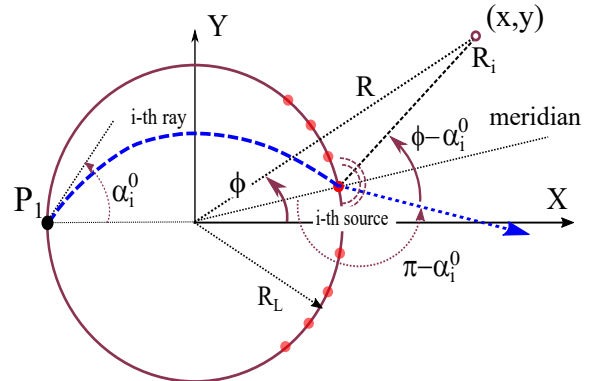

Fig. 2: Schematic representation of the ray tracing model outside the lens.

These equations allow to study any profile of a geodesic lens. It is common to set $R_L = 1.0$ without lack of generality.

B. Huygens' Secondary-Sources Array Model

Following an approach based on the Huygens-Fresnel principle and successfully validated in the case of PPW lenses [22], [40], a ray is modelled as a secondary point source when it reaches the aperture of the lens, so that the geodesic lens aperture is treated as a secondary-source array. The NF and the FF can be computed as the summation of the contribution of all these sources.

The feed of the lens is modelled by a point source from where the rays rise, forming up an angle α_i^0 ($0° \leq |\alpha_i^0| \leq \alpha_s \leq 90°$) with the meridian. Each ray travels through the lens a distance σ_i and arrives to the lens aperture at the point $\rho = R_L, \phi_i$, with an output angle $\theta_i = \alpha_i^0 - \phi_i$ with respect to the X-axis. The aperture becomes a point source array, where the electric field in the $Z = 0$ plane can be calculated as the sum of the contributions of all the rays. Each point is modelled as a source with a $cos(\phi)$ radiation pattern. The amplitude of each point source, $P'(\alpha_i^0)$, can be modelled using a ray-tube approximation with a regular distribution of rays as in [22]:

$$P'(\alpha_i^0) \propto \frac{P(\alpha_i^0)}{\sqrt{(x_{i+1} - x_{i-1})^2 + (y_{i+1} - y_{i-1})^2}} =$$

$$\propto \frac{P(\alpha_i^0)}{2R_L \sqrt{1 - \cos(\phi_{i+1} - \phi_{i-1})}} \quad (8)$$

where $P(\alpha)$ is the angular amplitude distribution function of the feed. Summing up all contributions, the electric field in a point (x, y) outside the geodesic lens can be calculated as:

$$E_z(x, y, 0) \propto \sum_{i=1}^{n} P'(\alpha_0^i) \cdot \frac{e^{-jk_0(\sigma_i + R_i)} \cdot \cos(\phi - \alpha_i^0)}{R_i} \quad (9)$$

$$R_i = \sqrt{(x - R_L \cos\phi_i)^2 + (y - R_L \sin\phi_i)^2)} \quad (10)$$

where k_0 is the phase constant in the air.

In this paper, we have assumed a field distribution for the feed $\cos^q(\alpha)$ with $q = 2.3$.

C. Focusing Geodesic Lens

In order to focus the rays in the point $P_2[\rho_2, \phi_2]$, the shape of the geodesic lens can be determined using the function $s(\rho)$, written as in [44]:

$$s(\rho) = A(\rho)\rho + B \cdot R_L \arcsin(\rho/R_L) + C(\rho), \quad (11)$$

where

$$A(\rho) = 1 - \frac{1}{\pi} \arcsin \sqrt{\frac{R_L^2 - \rho^2}{\rho_1^2 - \rho^2}} - \frac{1}{\pi} \arcsin \sqrt{\frac{R_L^2 - \rho^2}{\rho_2^2 - \rho^2}} \quad (12)$$

$$B = (M - 1) + \frac{1}{\pi} \arcsin \frac{R_L}{\rho_1} + \sqrt{\rho_1^2 - R_L^2}$$

$$+ \frac{1}{\pi} \arcsin \frac{R_L}{\rho_2} + \sqrt{\rho_2^2 - R_L^2} \quad (13)$$

$$C(\rho) = -\frac{\rho_1}{\pi} \arcsin \sqrt{\frac{\rho \cdot (\rho_1^2 - R_L^2)}{R_L \cdot (\rho_1^2 - \rho^2)}}$$

$$- \frac{\rho_2}{\pi} \arcsin \sqrt{\frac{\rho \cdot (\rho_2^2 - R_L^2)}{R_L \cdot (\rho_2^2 - \rho^2)}} \quad (14)$$

where M is a non-negative real number such that $-\pi M$ corresponds to the total change of polar angle in radians swept by the light ray during its propagation. If the feed is at $P_1(\rho_1, -\pi)$, then $M = \phi_2/\pi$. For a Luneburg lens ($\rho_2 = \infty$), A and B are equal to $1/2$. For a Maxwell's fish-eye lens ($\rho_2 = 1 \cdot R_L$), $A = 0$ and $B = 1$. As an example, Fig. 3. shows the ray tracing of a GL with $\rho_1 = 1.1 \cdot R_L$, $\rho_2 = 2.0 \cdot R_L$ and $M = 1.05$. This lens focuses the rays in two different points. Since $\rho_1 > 1.0 \cdot R_L$, this lens has spillover radiation, illustrated in Fig. 3 with two rays that escape the lens in the source side. Looking at eq. 1, if $\rho_1 > R_L$, the maximum value of α is $\alpha_{max} = \arcsin(R_L/\rho_1)$. Spillover radiation appears for values $\alpha_{max} < \alpha < \pi/2$ and the spillover power P_{spill} can be calculated as:

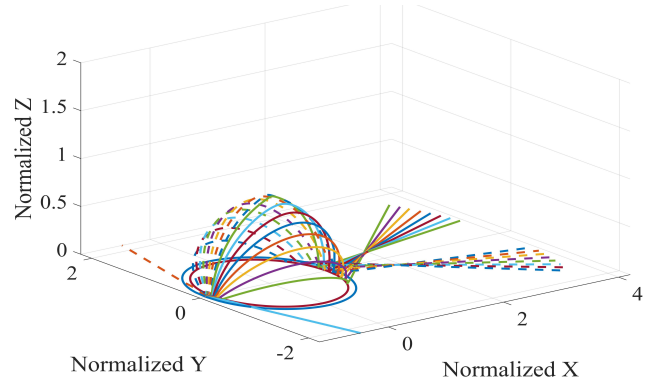$$P_{spill} = \int_{\alpha_{max}}^{\pi/2} P(\alpha)d\alpha \quad (15)$$

Fig. 3: Ray tracing of a focusing geodesic lens with $\rho_1 = 1.1 \cdot R_L$, $\rho_2 = 2.0 \cdot R_L$ and $M = 1.05$. Dimensions are normalized to the diameter of the lens.

D. Model Validation

The Huygens' secondary-sources array method has been used to analyze the modulated GLA proposed in [39]. This work proposed an equivalent planar lens model to compute the field distribution in the aperture of the lens, used in the array model to analyze the radiation pattern. The function $s(\rho)$ can be derived from eq. (9) of [39] using this specific design for the validation of the method described in this paper. In Fig. 4, we illustrate the comparison between measurements, full-wave simulation using ANSYS HFSS [46] and both analytical models: (i) the equivalent planar model proposed in [39], and (ii) the true-ray model proposed in this paper. Both analytical models have similar results, with only small differences mostly attributed to sampling effects. They both predict well the main beam shape and overall side lobe level, with some deviation in the nulls due to secondary effects not accounted for in

the simplified models, such as small unwanted reflections in bends and port-to-port coupling. The agreement remains however fairly acceptable and in line with the purpose of an optimization tool as described in [39]. Additionally, a true-ray tracing in the analyzed modulated lens is shown in Fig. 5, illustrating the good collimating properties of the design.
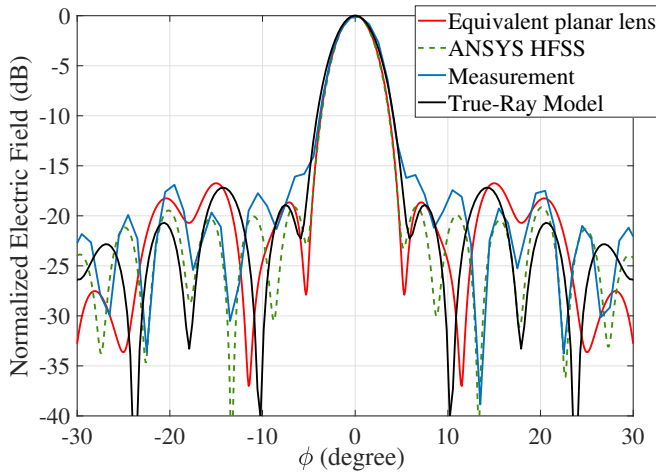

Fig. 4: Radiation patterns for the modulated geodesic lens in [39] compared to the results of the true-ray model proposed in this work.
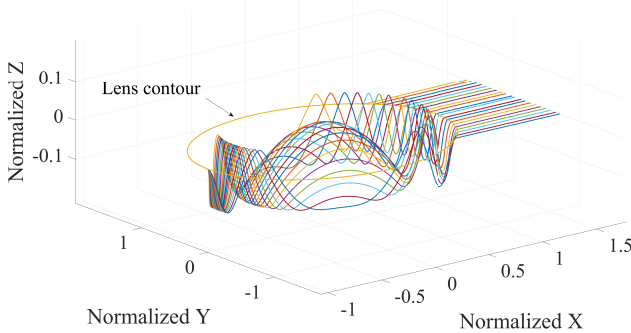

Fig. 5: True ray tracing of the modulated geodesic lens in [39].

III. ENHANCED AGGREGATE GAIN GEODESIC LENS ANTENNA DESIGN

A. Multibeam Geodesic Lens Design

The model described in section II has been applied to design an antenna with enhanced coverage characteristics. The overlapping between adjacent beams in previously reported Rinehart-Luneburg lens antennas is approximately 7 dB [38] and 8 dB [39]. This leads to a degraded performance for some users within the field of view. A possible workaround is to use two lenses with interleaved beams as described in [23]. However, this approach requires to duplicate hardware. The approach suggested here provides improved coverage characteristics using a single lens thanks to the wider beams

that the antenna generates. Previously reported antennas had a beamwidth of 8º and 5º with side lobe level (SLL) below -16 dB and -18 dB. Our target is a beamwidth wider than 20º and SLL below -15 dB, for a GLA with $R_L = 4 \cdot \lambda$ at 30 GHz (the same dimensions as in [38]), with $\rho_1 = 1.03 \cdot R_L$. To do so, we iteratively run the algorithm introduced in Section II monitoring the FF to match our requirements. This algorithm requires less than one minute in a conventional desktop computer to calculate the radiation pattern of the GLA with the aforementioned dimensions, while full-wave simulations performed with a commercial software such as CST or HFSS require around 20 minutes.

Therefore, it was very fast to optimize the lens for different values of ρ_2 and M with our method. A defocused lens with wider beamwidth and low SLL, fulfilling the design goals, was achieved for $\rho_2 = 2.9 \cdot R_L$ and $M = 1.004$. The normalized lens profile is shown in Fig. 6.a. Although in theory geodesic lenses are frequency independent, the distance between the top and bottom plates determines the bandwidth of operation in a parallel plate implementation. The distance between the plates has to be less than $\lambda/4$ so only the fundamental TEM mode propagates. To point the flare in the radial direction, a curved transition is inserted at the lens's outer rim. This transition was designed to ensure that the rays path do not get altered and that the reflections are kept to a minimum. Next, a flare was added to match the antenna to free space and to increase its gain. The flare is 15 mm in length and 5.74 mm in height. The lens was also simulated with ANSYS HFSS for a final check of our model. These results are represented in Fig. 7, where also the radiation pattern of a Luneburg lens was simulated to put in perspective the wider beams of the design we present.

A GL antenna has been constructed based on this profile. Seven ports were added to excite the lens (Fig. 6.b). The ports are not equidistant, but their separation has been slightly varied (20.0º, 17.0º and 18.5º, Fig. 6.b) to minimize the crossover between beams, which is at 2 dB below the maximum for all cases. In theory, an equidistant spacing should provide the desired performance over the field of view, owing to the rotational symmetry of the design. However, in practice, the finite size of the aperture leads to some truncation effects and associated small variations of the radiation patterns with the azimuth angle, hence, the need to adjust the spacing between the feeds to compensate for these variations. The simulated radiation pattern for each port is illustrated in Fig. 8. Each beam has been normalized to its maximum. Due to the inherent circular symmetry of the GL, all the beams fulfill a minimum 24º of beamwidth and a SLL below -15 dB.

A prototype was manufactured in two parts using CNC milling with a tolerance of 0.1 mm. A photograph of the prototype is provided in Fig. 9. The waveguide-to-coaxial line transition was designed similarly to the one proposed in [38].

The S-parameters of the antenna have been measured. The reflection coefficients are below -10 dB at the main frequency of operation, between 29 GHz and 38 GHz, for all ports. All the S_{XY} parameters are below -30 dB, including coupling between ports 1 and 7, that are opposite to each other, and any coupling between adjacent ports.
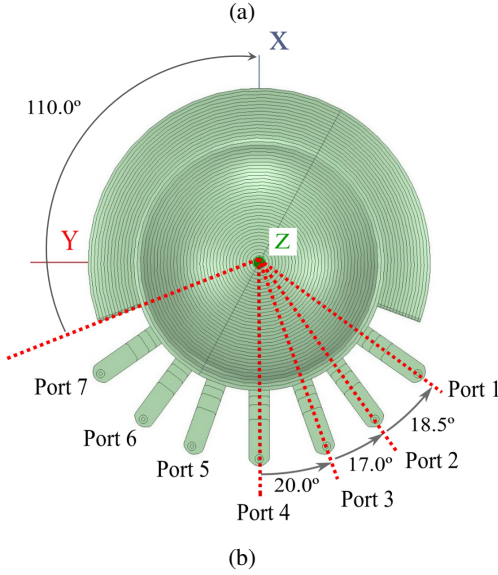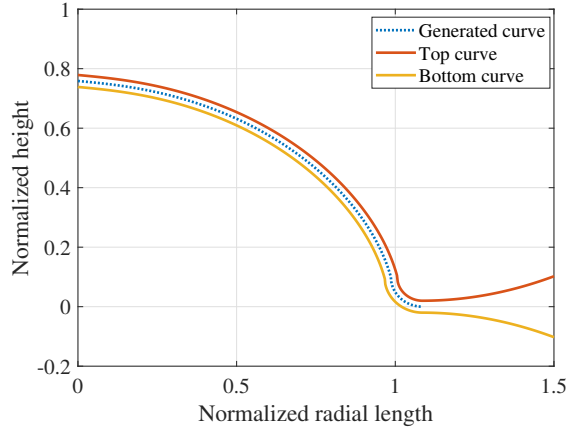
(a)

(b)

Fig. 6: (a) Profile of a GL with $\bar{\rho}_1 = 1.03$, $\bar{\rho}_2 = 2.9$ and $M = 1.004$. (b) Top view of the simulated GLA.
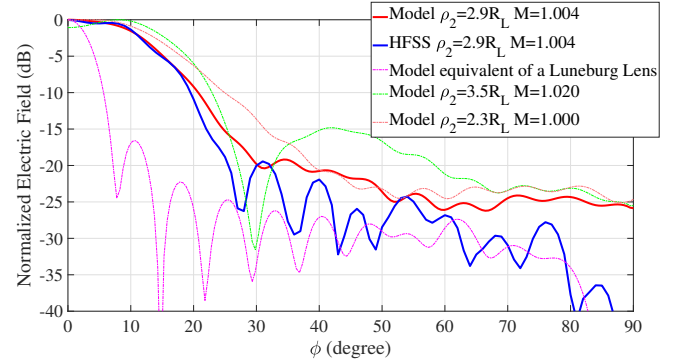

Fig. 7: Comparison of radiation patterns for various lenses using the model proposed and HFSS pattern (blue line) of the final design.

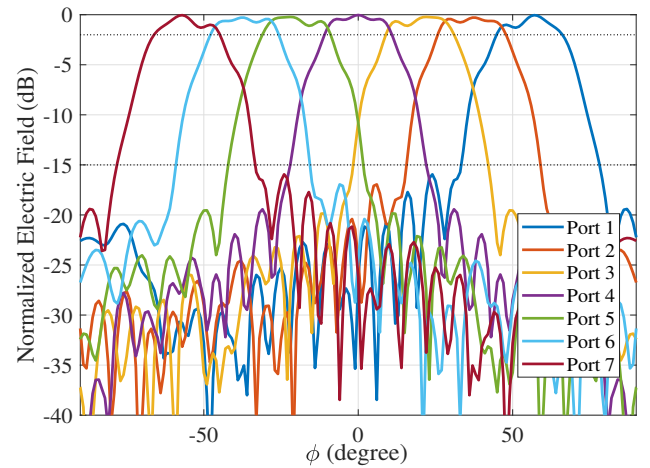Fig. 8: Far field radiation patterns of the NF focusing GLA with 7 independent ports.

B. Near-Field Measurements

The designed antenna is able to focus the energy in the NF. The NF characteristics of the antenna will determine the FF radiation patterns. Therefore, we wanted to validate our assumptions between the NF-to-FF features. To do so, the GLA was measured with a NF planar scanner at the facilities of the University of Oviedo, using an open-ended waveguide as probe. No probe compensation has been implemented. For each measurement, the unused ports were connected to 50 Ω loads. The NF of the GLA antenna was computed for port 4 using our model, as illustrated in Fig. 10.a. The corresponding measured NF for this port is shown in Fig. 10.b. In both cases, the fields are normalized to the value at $X = 80$ mm, $Y = 0$ mm. Good agreement between our model and measurements is found. Although the lens is not able to create a focusing spot at a given distance, it concentrates the intensity of the field in a beam. More information about NF beams for a focusing Rinehart-Luneburg GLA (with parameters $\rho_2 = \infty$) can be found in [45].

In Fig. 11, the measured NF is illustrated for each port,

without probe compensation. The GLA created a set of NF beams which are very similar due to the rotational symmetry of the lens. In Fig. 12, the normalized electric field is compared along a circular cut of 120 mm radius for our model, HFSS simulations and measurements (yellow circles in Fig. 11). These seven beams have an equal width up to -15 dB, showing slight differences in SLLs. The 3 dB beamwidth has a value below 7°.

C. Far-Field Measurements

The manufactured GLA was also measured in the spherical range anechoic chamber at the University of Oviedo (as illustrated in Fig. 13). A standard pyramidal horn antenna has been used as probe. This probe was located at a distance of 5.1 m. At this distance, the GLA is in FF, considering an aperture equal to the lens diameter (120 mm = 12 λ at 30 GHz). It is worth mentioning that the closer the focal point to the aperture, the closer the rays are to each other, as it can be seen in Fig. 3, and therefore, the smaller the aperture efficiency. The rays do not take advantage of the full aperture and; hence, a decrease in the directivity of the beams may

Fig. 9: Inside view of the two parts composing the GLA prototype.

Fig. 11: NF measurements of the electric field when each port of the GLA is excited. Contour limits: -18, -21, -24, -27, -30 and -33 dB.
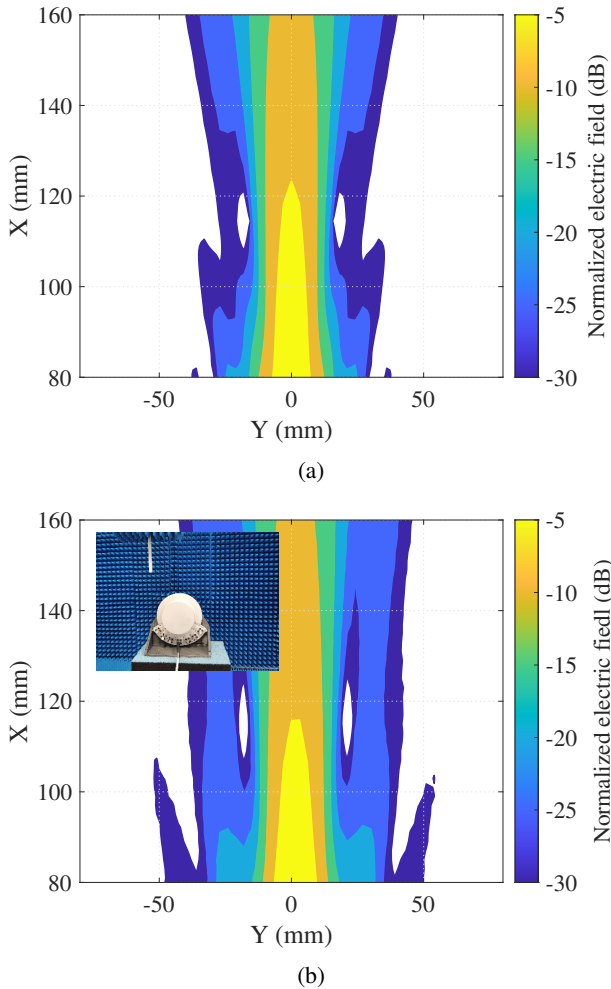

(a)

(b)

Fig. 10: Normalized NF of the designed GLA: (a) Model (b) Measurement. Inset: GLA in the NF measurement set-up.

appear. The gain in simulations and measurements for each ports are compared in Fig. 14. The maximum simulated gain is 13.4 dBi. Two black lines, 2 dB and 15 dB below that value, are drawn to show the performance of the measured antenna. It can be seen that between $\pm 67°$ the gain level of the antenna
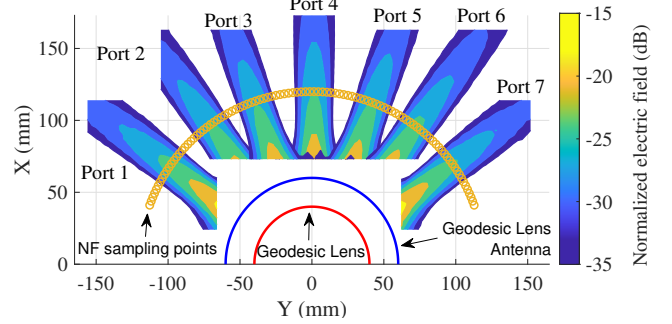
is above 11.4 dBi, ensuring stable aggregate gain over the field of view. The SLL are below -15 dB in almost all cases. Cross-polarization levels were also measured, and they were below -35 dB with respect to the maximum of the co-polarized field.

Fig. 15 shows the -1 dB, -2 dB and -3 dB contour plots in UV-coordinates ($U = \sin\Theta\sin\Phi$ and $V = \sin\Theta\cos\Phi$) for two different frequencies (30 and 35 GHz), where Θ is the angle between the direction under test and the X-axis; and Φ is the angle between the projection of the direction under test in the YZ-plane and the Z-axis. The resulting beams have a highly elliptical shape. For the 30 GHz case, -2 dB and -3 dB contours of two adjacent antennas overlap and no blank area exists inside the coverage zone below -2 dB. A -2 dB coverage area (purple line) of an antenna with a -2 dB beamwidth of 134º in the H-plane and 40º for the E-plane is drawn to facilitate the understanding of the coverage area. The antenna was not optimized for the 35 GHz case. At this frequency, the -2 dB beamwidth decreases for all beams. However, a wide area with coverage greater than -3 dB is maintained.

The frequency behavior of the antenna has been measured for the seven ports. Fig. 16 shows the contour plot of the normalized FF pattern (H-plane cut) as a function of the elevation angle and the frequency. Excellent angle stability and symmetry were obtained in all cases. When the frequency increases, the power in the center of the beam decreases between -2 dB and -4 dB. In this antenna, the focusing point approaches the lens at higher frequency and the rays increase the crossing angle.

Finally, table I provides a comparison with other reported mmWave designs with rotational symmetry and our presented work. In [47], only one port is used to design a flat beam with a field of view of $120°$. The Luneburg lens antennas studied in [38], [40] present greater gain and [38], [39] lower SLL, but the crossover is greater than 7 dB in all cases. In [19] and [43], the beamwidth has been increased to reduce the crossover. Although [19] presents a field of view greater than this work, the antenna gain decreases from $60°$. Thus, our design represents a good compromise between physical characteristics (size, number of ports) and electromagnetic performance, especially in terms of SLL and crossover. The lens radius or/and the flare height may be set to larger values to increase the antenna gain while maintaining the same radiation
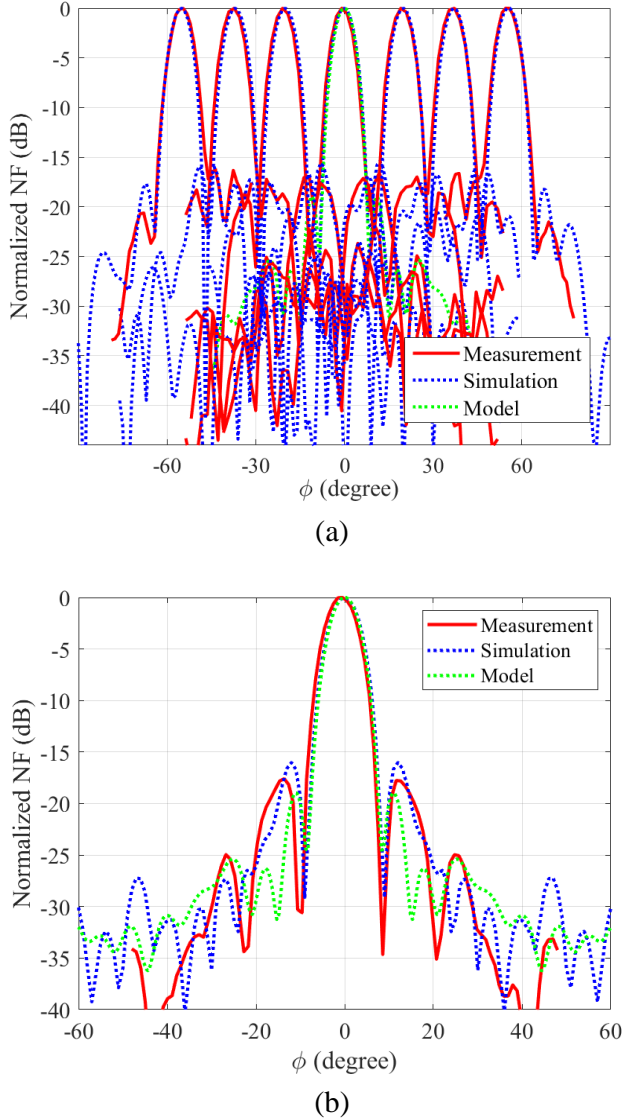
(a)

(b)

Fig. 12: (a) Comparison between the proposed model, HFSS and measurement results of the normalized NF beams for the GLA at a 120 mm radius corresponding with the NF sampling points in Fig. 11. (b) Zoom in the broadside beam.

characteristics. On the other hand, the profile of the lens can also be modified to generate more directive beams, similar to a Luneburg lens. This alternative has the drawback of increasing the crossover between adjacent beams and, in turn, increasing the gain variations across the field of view of the antenna.

IV. CONCLUSION

In this paper, we proposed a model which evaluates the radiation patternsof a rotationally symmetric geodesic lens based on ray-tracing. This method was used to find the profile of a NF focusing GL with a beamwidth of 24º in the FF in the H-Plane, with SLL below -15 dB at 30 GHz. This lens has been used to produce a multibeam antenna in which a trade-off of the feeding positions has been reached to
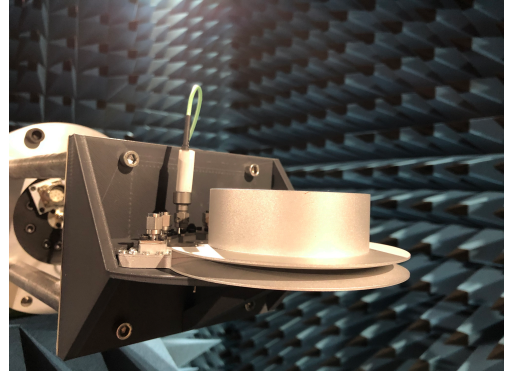

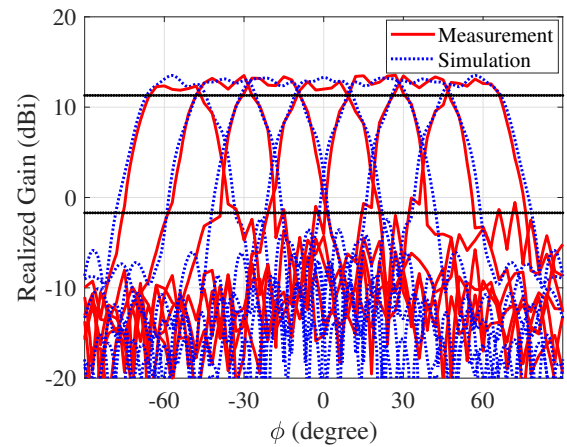Fig. 13: GLA prototype in the anechoic chamber at the University of Oviedo.

Fig. 14: Comparison between simulations and measurements of the realized gain in the H-plane when exciting the seven ports of the designed GLA.
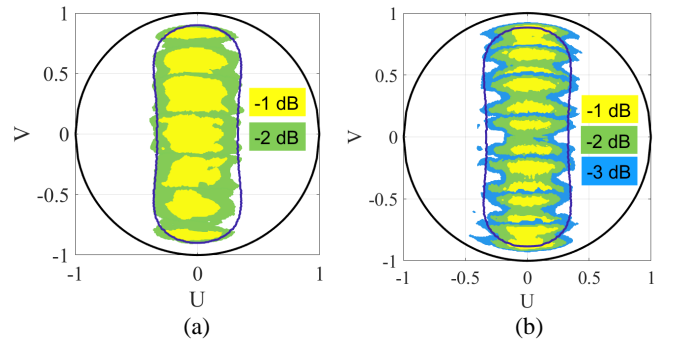
Fig. 15: 2-D contour of the aggregate radiation patterns of the designed GLA. (a) 30 GHz. (b) 35 GHz.

maximize coverage. The antenna was experimentally tested demonstrating an excellent agreement with the model. In the near-field, The GLA presents a spot-width of 7º at the focus distance (120 mm) for seven beams. In the far-field, all the beams present a gain greater than 13.4 dBi. The antenna has 134º of angular coverage, with a ripple better than 2 dB at 30 GHz. At 35 GHz, the antenna coverage is similar, but the

TABLE I: Main parameters of different reference designs compared to the proposed GLA.

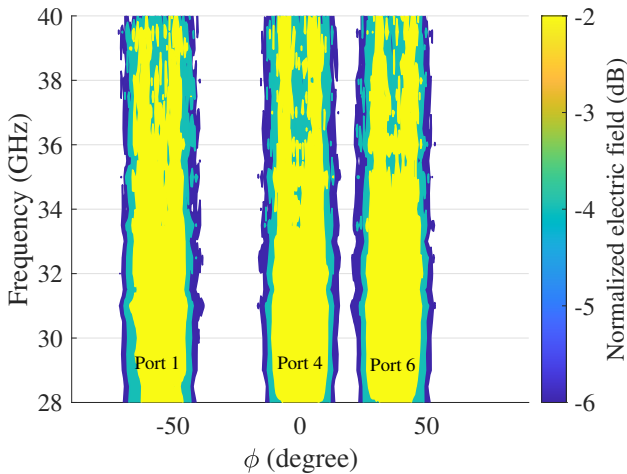| Work	Freq. [GHz]	Diameter [mm]	No. of ports	Gain (dB)	Beamwidth [°]	SLL [dB]	Crossover [dB]	Field of view [°]
[19]	30	100	21	16.8	8.6	-20	3.0	±80
[38]	28	117	11	17.3	8.0	-20	10.0	±62.5
[39]	30	150	21	23.8	7.5	-16	9.0	±75
[40]	30	150	10	23.3	7.5	-8.5	11.5	±33.75
[43] (meas.)	38	106	5	12.5	18.7	-8	1.0	±30
[47]	60	180	1	17.0	2.3	-9	N/A	N/A
This work	**30**	**120**	**7**	**13.4**	**24.0**	**-15**	**2.0**	**±67**

Fig. 16: Normalized radiation patterns as a function of elevation angle and frequency. Contour plots are drawn for -2 dB (yellow), - 4 dB (green) and -6 dB (blue).

crossover between adjacent beams is at -3 dB. The antenna has been also tested at higher frequencies, showing excellent angular stability, although with a decay in the electric field for the beam center. This antenna solution provides a more uniform gain across the service area, which is of interest for future mmWave wireless communication systems.

REFERENCES

[1] "5G wireless access: an overview," Ericsson AB, White Paper, April 2020. [Online]. Available: https://www.ericsson.com/498a10/assets/local/reports-papers/white-papers/whitepaper-5g-wireless-access.pdf
[2] "Ericsson Mobility Report," Ericsson AB, White Paper, November 2020. [Online]. Available: https://www.ericsson.com/4adc87/assets/local/mobility-report/documents/2020/november-2020-ericsson-mobility-report.pdf
[3] S. K. et al., "Where, when, and how mmwave is used in 5G and beyond," IEICE Trans. Electron., vol. 100-C, pp. 790–808, 2017.
[4] "Ericsson Microwave Outlook," Ericsson AB, White Paper, October 2020. [Online]. Available: https://www.ericsson.com/4a811d/assets/local/reports-papers/microwave-outlook/2020/2020-ericsson-microwave-outlook-report-digital.pdf
[5] J. Zhang, X. Ge, Q. Li, M. Guizani, and Y. Zhang, "5G millimeter-wave antenna array: Design and challenges," IEEE Wirel. Commun., vol. 24, no. 2, pp. 106–112, 2017.
[6] M. H. Dahri, M. I. Abbasi, M. H. Jamaluddin, and M. R. Kamarudin, "A review of high gain and high efficiency reflectarrays for 5g communications," IEEE Access, vol. 6, pp. 5973–5985, 2018.
[7] O. Quevedo-Teruel, M. Ebrahimpouri, and F. Ghasemifard, "Lens antennas for 5G communications systems," IEEE Commun. Mag., vol. 56, no. 7, pp. 36–41, 2018.
[8] W. Hong et al., "Multibeam antenna technologies for 5G wireless communications," IEEE Trans. Antennas Propag., vol. 65, no. 12, p. 6231–6249, 2017.
[9] E. L. Holzman, "Pillbox antenna design for millimeter-wave base-station applications," IEEE Antennas Propag. Mag., vol. 45, no. 1, pp. 27–37, Feb. 2003.
[10] M. Ettorre, R. Sauleau, and L. Le Coq, "Multi-beam multi-layer leaky-wave siw pillbox antenna for millimeter-wave applications," IEEE Trans. Antennas Propag., vol. 59, no. 4, pp. 1093–1100, Apr. 2011.
[11] E. Gandini et al., "Siw slotted waveguide array with pillbox transition for mechanical beam scanning," IEEE Antennas Wirel. Propag. Lett., vol. 11, 2012.
[12] Y. J. Cheng et al., "Substrate integrated waveguide (SIW) rotman lens and its Ka-band multibeam array antenna applications," IEEE Trans. Antennas Propag., vol. 56, no. 8, pp. 2504–2513, Aug. 2008.
[13] W. Lee, J. Kim, and Y. J. Yoon, "Compact two-layer rotman lens-fed microstrip antenna array at 24 GHz," IEEE Trans. Antennas Propag., vol. 59, no. 2, pp. 460–466, Feb. 2011.
[14] N. Jastram and D. S. Filipovic, "Design of a wideband millimeter wave micromachined rotman lens," IEEE Trans. Antennas Propag., vol. 63, no. 6, pp. 2790–2796, June 2015.
[15] K. Tekkouk et al., "Multibeam siw slotted waveguide antenna system fed by a compact dual-layer rotman lens," IEEE Trans. Antennas Propag., vol. 64, no. 2, pp. 504–514, Feb. 2016.
[16] C. Pfeiffer and A. Grbic, "A printed, broadband luneburg lens antenna," IEEE Trans. Antennas Propag., vol. 58, no. 9, pp. 3055–3059, Sept. 2010.
[17] A. B. Numan, J.-F. Frigon, and J.-J. Laurin, "Printed W-band multibeam antenna with luneburg lens-based beamforming network," IEEE Trans. Antennas Propag., vol. 66, no. 10, pp. 5614–5619, Oct. 2018.
[18] K. Wu, M. Bozzi, and N. J. G. Fonseca, "Substrate integrated transmission lines: review and applications," IEEE J. Microwaves, vol. 1, no. 1, pp. 345–363, Jan. 2021.
[19] C. Hua, X. Wu, N. Yang, and W. Wu, "Air-filled parallel-plate cylindrical modified luneberg lens antenna for multiple-beam scanning at millimeter-wave frequencies," IEEE Trans. Microw. Theory Tech., vol. 61, no. 1, pp. 436–443, 2013.
[20] V. Basavarajappa, A. Pellon, I. Montesinos-Ortego, B. B. Exposito, L. Cabria, and J. Basterrechea, "Millimeter-wave multi-beam waveguide lens antenna," IEEE Trans. Antennas Propag., vol. 67, no. 8, pp. 5646–5651, 2019.
[21] F. Doucet, N. J. G. Fonseca, E. Girard, H. Legay, and R. Sauleau, "Analysis and design of a continuous parallel plate waveguide multiple beam lens antenna at ku-band," 11th European Conf. Antennas Propag. (EuCAP), Paris, France, pp. 3631–3635, 2017.
[22] F. Doucet, N. J. G. Fonseca, E. Girard, H. Legay, and R. Sauleau, "Analytical model and study of continuous parallel plate waveguide lens-like multiple beam antennas," IEEE Trans. Antennas Propag., vol. 66, no. 9, pp. 4426–4436, 2018.
[23] F. Doucet et al., "Shaped continuous parallel plate delay lens with enhanced scanning performance," IEEE Trans. Antennas Propag., vol. 67, no. 11, pp. 6695–6704, 2019.
[24] S. Maci, G. Minatti, M. Casaletti, and M. Bosiljevac, "Metasurfing: Addressing waves on impenetrable metasurfaces," IEEE Antennas Wirel. Propag. Lett., vol. 10, pp. 1499–1502, 2011.
[25] O. Quevedo-Teruel, M. Ebrahimpouri, and M. N. M. Kehn, "Ultrawideband metasurface lenses based on off-shifted opposite layers," IEEE Antennas Wirel. Propag. Lett., vol. 15, pp. 484–487, 2016.
[26] C. D. Diallo, E. Girard, H. Legay, and R. Sauleau, "All-metal ku-band luneburg lens antenna based on variable parallel plate spacing fakir bed," 11th European Conf. Antennas Propag. (EuCAP), Paris, France, pp. 1401–1404, 2017.

[27] O. Quevedo-Teruel, J. Miao, M. Mattsson, A. Algaba-Brazalez, M. Johansson, and L. Manholm, "Glide-symmetric fully-metallic luneburg lens for 5g communications at ka-band," *IEEE Antennas Wirel. Propag. Lett.*, vol. 17, no. 9, pp. 1588–1592, 2018.

[28] P. Bantavis, C. G. Gonzalez, R. Sauleau, G. Goussetis, S. Tubau, and H. Legay, "Broadband graded index gutman lens with a wide field of view utilizing artificial dielectrics: a design methodology," *Opt. Express*, vol. 28, no. 10, pp. 14 648–14 661, May 2020.

[29] R. K. Luneburg, "Mathematical theory of optics," *Providence, Brown University Press*, 1944.

[30] N. J. G. Fonseca, "A focal curve design method for Rotman lenses with wider angular scanning range," *IEEE Antennas Wirel. Propag. Lett.*, vol. 16, pp. 54–57, 2017.

[31] Z. Zhang, S. Yang, Y. Chen, S. Qu, and J. Hu, "Fast analysis of parallel-plate cylindrical luneberg lens antennas through dyadic green's functions," *IEEE Transactions on Microwave Theory and Techniques*, vol. 66, no. 10, pp. 4327–4337, 2018.

[32] S. Adachi, R. Rudduck, and C. Walter, "A general analysis of nonplanar, two-dimensional luneberg lenses," *IRE Transactions on Antennas and Propagation*, vol. 9, no. 4, pp. 353–357, 1961.

[33] R. Rudduck and C. Walter, "A general analysis of geodesic luneberg lenses," *IRE Transactions on Antennas and Propagation*, vol. 10, no. 4, pp. 444–449, 1962.

[34] R. Rudduck, C. Ryan, and C. Walter, "Beam elevation positioning in geodesic lenses," *IEEE Transactions on Antennas and Propagation*, vol. 12, no. 6, pp. 678–684, 1964.

[35] G. Thiele and R. Rudduck, "Geodesic lens antennas for low-angle radiation," *IEEE Transactions on Antennas and Propagation*, vol. 13, no. 4, pp. 514–521, 1965.

[36] R. F. Rinehart, "A solution of the problem of rapid scanning for radar antennae," *J. Appl. Phys.*, vol. 19, p. 860–862, Sept. 1948.

[37] R. F. Rinehart, "A family of designs for rapid scanning radar antennas," *Proc. IRE*, vol. 40, p. 686–688, June 1952.

[38] Q. Liao, N. J. G. Fonseca, and O. Quevedo-Teruel, "Compact multibeam fully-metallic geodesic luneburg lens antenna based on non-euclidean transformation optics," *IEEE Trans. Antennas Propag.*, vol. 66, no. 12, pp. 7383–7388, 2018.

[39] N. J. G. Fonseca, Q. Liao, and O. Quevedo-Teruel, "Equivalent planar lens ray tracing model to design modulated geodesic lenses using non-euclidean transformation optics," *IEEE Trans. Antennas Propag.*, vol. 68, no. 5, pp. 3410–3422, 2020.

[40] N. J. G. Fonseca, Q. Liao, and O. Quevedo-Teruel, "Compact parallel-plate waveguide half-luneburg geodesic lens in the Ka-band," *IET Microw. Antennas Propag.*, 2020.

[41] N. J. G. Fonseca, "The water drop lens: revisiting the past to shape the future," *EurAAP Reviews Electromagn.*, vol. I, 2022.

[42] H. Chou, Y. Chang, H. Huang, Z. Yan, T. Lertwiriyaprapa, and D. Torrungrueng, "Optimization of three-dimensional multi-shell dielectric lens antennas to radiate multiple shaped beams for cellular radio coverage," *IEEE Access*, vol. 7, pp. 182 974–182 982, 2019.

[43] H. Chou, Y. Chang, H. Huang, Z. Yan, T. Lertwiriyaprapa, and D. Torrungrueng, "Two-dimensional multi-ring dielectric lens antenna to radiate fan-shaped multi-beams with optimum adjacent-beam overlapping crossover by genetic algorithm," *IEEE Access*, vol. 8, pp. 79 124–79 133, 2020.

[44] M. Šarbort and T. Tyc, "Spherical media and geodesic lenses in geometrical optics," *J. Opt.*, vol. 14, no. 7, p. 075705, 2012.

[45] G. Leon, O. Orgeira, N. J. G. Fonseca, and O. Quevedo-Teruel, "Ray-tracing analysis of the near and far fields of focusing geodesic lens antennas," *14th European Conf. Antennas Propag. (EuCAP), Copenhagen, Denmark*, 2020.

[46] A. Corp., "Ansys® Electromagnetics Suite , release 2019 r1," Pittsburgh, PA. USA. 2018.

[47] Z. Zhang, S. Yang, Y. Zeng, S. Qu, and Y. Chen, "A cylindrical lens antenna with extremely flat beams," *IEEE Access*, vol. 7, pp. 156 675–156 685, 2019.